



# A penalty immersed boundary method for viscoelastic particulate flows

Yongsam Kim<sup>a,\*</sup>, Ming-Chih Lai<sup>b</sup>, Yunchang Seol<sup>c</sup>

<sup>a</sup> Department of Mathematics, Chung-Ang University, Dongjakgu Heukseokdong, Seoul 156-756, Republic of Korea

<sup>b</sup> Department of Applied Mathematics, Institute of Mathematical Modeling and Scientific Computing, National Chiao Tung University, 1001, Ta Hsueh Road, Hsinchu 300, Taiwan

<sup>c</sup> Shing-Tung Yau Center, 1001 University Road, National Chiao-Tung University, Hsinchu City 30010, Taiwan

## ARTICLE INFO

### Keywords:

Rigid particle  
Penalty idea  
Immersed boundary method  
Oldroyd-B fluid

## ABSTRACT

We extend the penalty immersed boundary (pIB) method to investigate the interaction between circular rigid particles and a surrounding viscoelastic Oldroyd-B fluid. The basic idea of the pIB method is the splitting of an immersed boundary, which here is a rigid body, notionally into two Lagrangian components: one is a massive component carrying all mass of the rigid body, and the other is massless. These two components are connected by a system of stiff springs with zero rest length. The massive component has no direct interaction with the surrounding fluid and behaves as though in a vacuum, following the dynamics of a rigid body, in which the acting forces and torques are generated from the system of stiff springs that connects the two Lagrangian components. The massless component interacts with the surrounding Oldroyd-B fluid: it moves at the local fluid velocity and exerts force locally on the fluid. We verify the pIB method combined with Oldroyd-B fluid model by investigating the effects of the wall and elasticity of the fluid on the lateral position of a circular particle falling under the influence of gravity and by studying convergence of the numerical solutions. We also simulate the interaction between multiple circular particles and the surrounding Oldroyd-B fluid and compare the dynamics of the particles in various flow conditions.

## 1. Introduction

We investigate the interaction between circular rigid particles and a surrounding non-Newtonian fluid. The motion of particles in non-Newtonian fluids is not only of theoretical interest, but is also important in many applications to industrial processes involving particle laden materials [1,2]. It is well known that, whereas an ellipse or a long particle falls with its broad side normal to the falling direction in a Newtonian fluid, it falls with its broad side parallel to the falling direction in a viscoelastic liquid [3,4]. Moreover, multiple particles, which are dropped in a channel, are lined up along the flow direction when the viscoelastic Mach number is less than 1 and the elasticity number is greater than 1 [5–7].

Compared to numerical methods for simulating particulate flows in Newtonian fluids which have been very successful, simulation methods for the motion of particulate flows in a viscoelastic fluid is still complicated and challenging. There have been recent works on the simulation of the sedimentation of particles in viscoelastic fluids, such as Oldroyd-B fluids [3,5–9], Oldroyd-B fluids with shear thinning [3,10], and viscoelastic fluids of the FENE-Dumbbells model [11]. Feng et al. [8] used the finite element method to study the 2D sedimentation of circular particles in an Oldroyd-B fluid and obtained chains of two particles aligned

with the direction of sedimentation, which was observed in the actual experiments [12]. The authors in [3] used an arbitrary Lagrangian–Eulerian (ALE) moving mesh technique to investigate the cross-stream migration and orientations of elliptic particles in Oldroyd-B fluids with and without shear thinning. In [5], a fictitious domain/distributed Lagrange multiplier method for particulate flow of Oldroyd-B fluids was developed for fixed structured mesh to observe chains of two particles aligned with the direction of sedimentation. Yu et al. in [10] developed a different fictitious domain/distributed Lagrange multiplier method with finite difference methods to investigate the sedimentation of particles in an Oldroyd-B fluid with shear thinning.

We here combine the idea of the penalty immersed boundary (pIB) method and a finite difference Oldroyd-B fluid solver to investigate the interaction between circular rigid bodies and a surrounding viscoelastic Oldroyd-B fluid. The immersed boundary (IB) method has been widely used to investigate the problems in which an elastic boundary or body is immersed in and interacts with a surrounding Newtonian fluid [13–15]. Kim and Peskin [16,17] have introduced an extension of the IB method which can easily handle an elastic boundary or a rigid body with mass. We call it the penalty immersed boundary (pIB) method and have shown in [16,17] that the pIB method can be applied to many problems in which mass of the elastic boundary or rigid body plays an

\* Corresponding author.

E-mail addresses: [kimy@cau.ac.kr](mailto:kimy@cau.ac.kr) (Y. Kim), [mclai@math.nctu.edu.tw](mailto:mclai@math.nctu.edu.tw) (M.-C. Lai), [ycseol@ntu.edu.tw](mailto:ycseol@ntu.edu.tw) (Y. Seol).

important dynamical role. For more examples of the application of the pIB method, see [18–20].

The pIB idea for a rigid body in Newtonian or Oldroyd-B fluid uses two representations for a rigid body: a massless component and a massive component which are connected by stiff springs. The massless component moves at the local fluid velocity and exerts force locally to the fluid. The force that it applies to the fluid is the force generated from the stiff springs that link it to its massive counterpart. On the other end of the spring, the massive component moves as though in a vacuum following the dynamics of a rigid body in which forces and torques acting on the massive component are the gravitational force and those generated from the springs that connect it to the massless counterpart [17].

In the pIB method, we separate the dynamics of a rigid body only through a system of stiff springs from the whole system that, otherwise, would strongly couple the rigid body dynamics to the fluid dynamics (here, Oldroyd-B fluid) through constraints. By doing that, we allow the equations for the fluid motion itself to be as simple as possible. Particularly, we keep the density of the fluid equations to be uniformly constant. As the stiffness of the springs that link the massless component to the massive component goes to infinity, the massive component accompanies the massless component and provides it with mass. For the quantitative verification of this behavior, see [16].

There are two kinds of direct numerical methods often used to simulate the viscoelastic particulate flows involving full fluid equations: one is to use the dynamic and kinematic boundary conditions to interact the rigid body dynamics with fluid dynamics [3,8,9,21]. This method needs projection and remeshing techniques since the body is moving, and requires an iterative method to update the fluid velocity, and the translational and angular velocities of the body. The second type of methods is to imbed the rigid body into a simple fluid domain and to give some constraints for rigid body motion on the particle region. Our present pIB method and the distributed Lagrange multiplier/fictitious domain method are in this category. Whereas the latter uses the distributed Lagrange multiplier to enforce the constraint on the rigid body motion [5,7,10,22], the pIB method uses the penalty force which is generated from the stiff springs connecting the two Lagrangian descriptions of the rigid body.

In order to verify that the present pIB method for viscoelastic particulate flows is a robust and efficient numerical technique to simulate a rigid body interacting with a surrounding Oldroyd-B fluid, we simulate a freely falling circular particle in an Oldroyd-B fluid with which we perform a convergence study to show that the pIB method is first-order accurate and investigate the effects of wall and elasticity on the lateral equilibrium position of the descending particle. We also study the interaction of multiple (two, three, and six) circular particles falling in a channel filled with an Oldroyd-B fluid and show that the particles form a chain that descends parallel to the flow when the elasticity number (or relaxation time) is large enough, which is well-known in literature.

## 2. Equations of motion

We consider a 2D viscoelastic incompressible fluid containing a rigid body which has two Lagrangian descriptions: one is denoted by  $\mathbf{X}(r, s, t)$  where  $(r, s)$  are curvilinear coordinates and  $t$  is time which has no mass and plays the same role as an immersed boundary in a more traditional IB method with massless boundary assumption, and the other, which we denote  $\mathbf{Y}(r, s, t)$ , carries all of the excess mass and is connected to  $\mathbf{X}(r, s, t)$  by a system of stiff springs, see the left picture of Fig. 1. The excess mass is the difference between the mass of the body and the mass of the fluid it displaces. The different points of the massive boundary  $\mathbf{Y}(r, s, t)$  have no direct connection to the fluid and move together as though a rigid body in a vacuum, with the only forces and torques applied on the body being the force of gravity, and those generated from the springs that connect the massless description to the massive description of the rigid body.

Let  $\rho$  and  $\mu_s$  be the fluid density and viscosity, respectively, then the equations of the motion for 2D Oldroyd-B fluid interacting with an immersed body are the following:

$$\rho \left( \frac{\partial \mathbf{u}}{\partial t} + (\mathbf{u} \cdot \nabla) \mathbf{u} \right) = -\nabla p + \mu_s \Delta \mathbf{u} + \nabla \cdot \mathbf{A} + \mathbf{f}, \quad (1)$$

$$\nabla \cdot \mathbf{u} = 0, \quad (2)$$

$$\frac{\partial \mathbf{A}}{\partial t} + (\mathbf{u} \cdot \nabla) \mathbf{A} - \nabla \mathbf{u} \mathbf{A} - \mathbf{A} (\nabla \mathbf{u})^T + \frac{1}{r_t} \mathbf{A} = \frac{2\mu_p}{r_t} \mathbf{d}(\mathbf{u}), \quad (3)$$

$$\mathbf{F}(r, s, t) = K(\mathbf{Y}(r, s, t) - \mathbf{X}(r, s, t)), \quad (4)$$

$$\mathbf{f}(\mathbf{x}, t) = \int \mathbf{F}(r, s, t) \delta(\mathbf{x} - \mathbf{X}(r, s, t)) dr ds, \quad (5)$$

$$\frac{\partial \mathbf{X}}{\partial t}(r, s, t) = \mathbf{u}(\mathbf{X}(r, s, t), t) = \int \mathbf{u}(\mathbf{x}, t) \delta(\mathbf{x} - \mathbf{X}(r, s, t)) d\mathbf{x}. \quad (6)$$

The equations of motion of the rigid body itself will be given later.

Eqs. (1)–(3) are the Oldroyd-B model for a viscoelastic fluid in which  $r_t$  is a relaxation time,  $\mu_p$  is the polymer contribution to the zero-shear-rate viscosity, and  $\mathbf{d}(\mathbf{u}) = \frac{1}{2}(\nabla \mathbf{u} + (\nabla \mathbf{u})^T)$  is the fluid deformation tensor. Here the unknowns are the velocity field,  $\mathbf{u}(\mathbf{x}, t)$ ; the fluid pressure,  $p(\mathbf{x}, t)$ ; the extra stress tensor ( $2 \times 2$  matrix),  $\mathbf{A}(\mathbf{x}, t)$ ; and the external force per unit area applied by the immersed body  $\mathbf{X}(r, s, t)$  to the fluid,  $\mathbf{f}(\mathbf{x}, t)$ . Note that the domain on which Eqs. (1)–(3) are defined includes the domain occupied by the rigid body. In the IB method, there is always fluid everywhere. Anything immersed in the fluid is regarded as a part of the fluid in which forces are applied and in which additional mass may be present.

Eq. (4) defines the force density  $\mathbf{F}$  which is applied by the massless component  $\mathbf{X}(r, s, t)$  of the immersed body to the fluid so that  $\mathbf{F}(r, s, t) dr ds$  is the force transmitted to the fluid by the area element  $dr ds$  of the body. The force density  $\mathbf{F}$  is generated by the stiff springs that connect the massive and massless descriptions of the immersed body. As the stiffness parameter  $K$ , which is called the “penalty” parameter of the method, gets large, the energy penalty increases that must be paid to separate the two descriptions  $\mathbf{Y}(r, s, t)$  and  $\mathbf{X}(r, s, t)$  by any given amount.

The interaction Eqs. (5) and (6) express the local character of the interaction through the two-dimensional Dirac delta function  $\delta(\mathbf{x}) = \delta(x)\delta(y)$ . Eq. (5) relates the two corresponding force densities  $\mathbf{f}(\mathbf{x}, t) d\mathbf{x}$  and  $\mathbf{F}(r, s, t) dr ds$ , which can be seen by integrating each side of Eq. (5) over an arbitrary region  $\Omega$ . Eq. (6) is the equation of motion of the massless component  $\mathbf{X}(r, s, t)$  of the immersed body. It simply says that the body  $\mathbf{X}(r, s, t)$  moves at the local fluid velocity, i.e., by no-slip condition.

If the force density  $\mathbf{F}$  in Eq. (4) were a function of the massless component  $\mathbf{X}(r, s, t)$  only, that is, if  $\mathbf{Y}(r, s, t)$  were given, then Eqs. (1)–(6) would be complete. However, since the force density  $\mathbf{F}$  is also a function of the unknown massive representative  $\mathbf{Y}(r, s, t)$  of the rigid body, we need to take into account the rigid-body dynamics. To do that, let  $\mathbf{Y}_{\text{cm}}(t)$  be the center of mass of the body and  $\{\mathbf{E}_1(t), \mathbf{E}_2(t)\}$  be the orthonormal basis for a coordinate system fixed to the body with its origin at the center of mass. Then we can write the position of the material point  $r, s$  of the body as

$$\begin{aligned} \mathbf{Y}(r, s, t) &= \mathbf{Y}_{\text{cm}}(t) + c_1(r, s) \mathbf{E}_1(t) + c_2(r, s) \mathbf{E}_2(t) \\ &= \mathbf{Y}_{\text{cm}}(t) + \mathcal{E}(t) \mathbf{C}(r, s), \end{aligned} \quad (7)$$

where  $\mathcal{E}(t)$  is a  $2 \times 2$  matrix of which the  $i$ th column is  $\mathbf{E}_i(t)$ , and  $\mathbf{C}(r, s)$  is a  $2 \times 1$  vector-valued function of which the  $i$ th component is  $c_i(r, s)$ . Since the coordinates are fixed to the body, the coefficients  $c_i(r, s)$ 's are independent of time. Note that Eq. (7) allows for general curvilinear coordinates  $r, s$  that are fixed to the body. We get the special case of Cartesian coordinates by setting  $c_1(r, s) = r$  and  $c_2(r, s) = s$ .

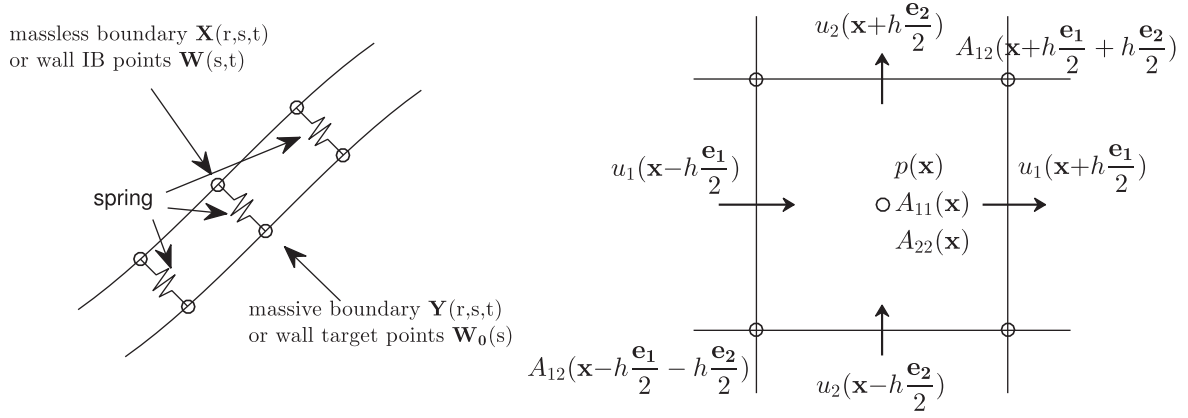


**Fig. 1.** Schematic view of massless boundary  $\mathbf{X}(r, s, t)$ , massive boundary  $\mathbf{Y}(r, s, t)$ , wall immersed boundary points  $\mathbf{W}(s, t)$ , and wall target boundary points  $\mathbf{W}_0(s)$  (left) in which the wall IB points (massless boundary) are connected to the wall target points (massive boundary) by a system of stiff springs with zero rest length. The staggered MAC grid in 2D (right) in which the fluid velocities are defined at the cell edges, the pressure and the diagonal elements of the extra stress tensor are defined at the cell centers, and the off-diagonal elements of the extra stress tensor are defined at the cell vertices [26].

Now the equations of motion of the rigid body  $\mathbf{Y}(r, s, t)$  are a dynamical system for the variables  $\mathbf{Y}_{\text{cm}}(t)$ ,  $\mathcal{E}(t)$ ,  $\mathbf{V}_{\text{cm}}(t)$ , and  $L(t)$ , where  $\mathbf{V}_{\text{cm}}(t)$  is the velocity of the center of mass and  $L(t)$  is the angular momentum of the body. These variables are expressed in the laboratory frame of reference. The equations for  $\mathbf{Y}_{\text{cm}}(t)$  and  $\mathbf{V}_{\text{cm}}(t)$  are

$$\frac{d\mathbf{Y}_{\text{cm}}}{dt} = \mathbf{V}_{\text{cm}}(t), \quad (8)$$

$$M \frac{d\mathbf{V}_{\text{cm}}}{dt} = - \int \mathbf{F}(r, s, t) dr ds - M g \mathbf{e}_2, \quad (9)$$

where  $\mathbf{F}$  is the restoring force in Eq. (4),  $\mathbf{e}_2$  is a unit vector in the positive  $y$  direction, and  $g$  is the gravitational acceleration. Here and in the following, any integral with respect to  $r, s$  is understood to extend over the whole of the immersed body. In Eq. (9),  $M$  is the excess mass of the body, i.e., the difference between its mass and the mass of the fluid displaced. Later on, we shall need the density of the excess mass, which we denote by  $m(r, s)$ . This is the difference between the density of the rigid body and the (constant) fluid density and, of course,  $M = \int m(r, s) dr ds$ . Note that the motion of  $\mathbf{Y}_{\text{cm}}(t)$  depends on only the gravitational force and the total force generated by the stiff springs that connect the massive and massless descriptions of the immersed body. Thus the massive body  $\mathbf{Y}(r, s, t)$  has no direct interaction with the surrounding fluid.

The rotational motion of the rigid body can be summarized as

$$T(t) = \int (\mathbf{Y}(r, s, t) - \mathbf{Y}_{\text{cm}}(t)) \times (-\mathbf{F}(r, s, t)) dr ds, \quad (10)$$

$$\frac{dL}{dt} = T(t), \quad (11)$$

$$\Omega(t) = L(t)/P_0, \quad (12)$$

$$\frac{d\mathbf{E}_i}{dt} = \mathcal{R}[\Omega(t)] \mathbf{E}_i(t), \quad i = 1, 2, \quad (13)$$

where  $T(t)$ ,  $L(t)$ , and  $\Omega(t)$  represent the total torque acting on the rigid body, its angular momentum, and the angular velocity, respectively. In (10), the cross product  $\mathbf{a} \times \mathbf{b}$  is the determinant of the matrix which has two column vectors  $\mathbf{a}$  and  $\mathbf{b}$ . In (13),  $\mathcal{R}[\theta]$  represents the orthogonal matrix that describes the rotation through the angle  $\theta$ , i.e.,

$$\mathcal{R}[\theta] = \begin{pmatrix} \cos \theta & -\sin \theta \\ \sin \theta & \cos \theta \end{pmatrix}. \quad (14)$$

In (12), the time-independent value  $P_0$ , which is called the initial moment of inertia, can be computed as  $P_0 = \int m(r, s) \mathbf{C}^T \mathbf{C} dr ds$ . For the

detailed derivations for the formula in 3D case, the readers can refer to Kim and Peskin [17].

The mathematical formulation of the pIB method for a two-dimensional viscoelastic fluid interacting with a rigid body is fully described by Eqs. (1)–(13). Consider the case in which  $K \rightarrow \infty$  in Eq. (4). Then the massless body  $\mathbf{X}(r, s, t)$  coincides with the massive body  $\mathbf{Y}(r, s, t)$  and obeys rigid-body kinematics. Even though  $K$  cannot be infinite in practice, we can choose  $K$  to be so large that  $\mathbf{Y}(r, s, t)$  and  $\mathbf{X}(r, s, t)$  move as closely as we like. However, a large value of  $K$  may generate computational instability, and thus there is a trade-off between the size of  $K$  and the time step restriction. This issue will be discussed in Section 4.1.

### 3. Numerical implementation

For the numerical implementation to solve Eqs. (1)–(13), we adopt a ‘formally’ second-order IB method which was used in [23,24] and generalize it to consider the dynamics of the massive body that is connected to the massless body by stiff springs [16–18]. This method is based on the framework of a second-order Runge–Kutta method in which each time step is divided into two substeps: the preliminary and final substeps. The preliminary substep computes data at time level  $n + \frac{1}{2}$  using data at time level  $n$  by a first-order accurate Euler method. Then the final substep uses the data at time levels  $n$  and  $n + \frac{1}{2}$  to update the data at time level  $n + 1$  by a second-order accurate midpoint rule.

Here we use a superscript to denote the time level. Let  $\Delta t$  be the time step,  $\mathbf{X}^n(r, s)$  is shorthand for  $\mathbf{X}(r, s, n\Delta t)$ , and all other variables can be written in similar shorthands. A subscript is used to denote the spatial discretization of the immersed body. Thus  $\mathbf{X}_k^n$ ,  $k = 1, \dots, N_b$ , denote the marker points representing the immersed body where  $N_b$  is the total number of points used in the discretization. We shall later use the notation  $\mathbf{X}_k^n = (X_{k,1}^n, X_{k,2}^n)$ .

Before describing the spatial and temporal iteration of the numerical scheme, we need the initialization of some variables. Initially the massive points  $\mathbf{Y}_k^0$  are exactly the same as the immersed body points  $\mathbf{X}_k^0$ , and the initial orthonormal frame  $\{\mathbf{E}_1^0, \mathbf{E}_2^0\}$  is chosen to be the standard basis for the 2D space. Then the corresponding orthonormal matrix  $\mathcal{E}^0$  is the  $2 \times 2$  identity matrix, and thus Eq. (7) determines the coordinates  $\mathbf{C}_k$  for the point  $\mathbf{Y}_k^0$  as  $\mathbf{C}_k = \mathbf{Y}_k^0 - \mathbf{Y}_{\text{cm}}^0$ , where  $\mathbf{Y}_{\text{cm}}^0$  is the center of mass of the body at time 0.

Let  $m_k$  be the excess mass density of the marker point  $\mathbf{X}_k^0$  of the body. Then the total excess mass  $M$  of the body can be computed as

$$M = \sum_{k=1}^{N_b} m_k \Delta r \Delta s, \quad (15)$$

where  $\Delta r$  and  $\Delta s$  are the spatial meshwidths for the immersed body. The initial moment of inertia  $P_0$  used in (12) is independent of time and can be computed as follows:

$$P_0 = \sum_{k=1}^{N_b} m_k \mathbf{C}_k^T \mathbf{C}_k \Delta r \Delta s. \quad (16)$$

### 3.1. Spatial discretizations for Oldroyd-B fluid

We discretize the physical domain by setting up a grid with meshwidth  $h = \Delta x_1 = \Delta x_2$  on which the fluid variables are defined. The grid of cell centers, denoted  $g_0$ , is given by

$$g_0 := \left\{ \left( \left( i + \frac{1}{2} \right) h, \left( j + \frac{1}{2} \right) h \right) \right\}, \quad (17)$$

where  $i = 0, \dots, N_x - 1$  and  $j = 0, \dots, N_y - 1$ . Here we use a staggered marker-and-cell (MAC) grid [25] in which the fluid velocity  $\mathbf{u} = (u_1, u_2)$  are defined at the cell faces, the pressure  $p$  and the diagonal elements of the extra stress tensor  $\mathbf{A}$  are defined at the cell centers, and the off-diagonal elements of  $\mathbf{A}$  are defined at the cell vertices [26]. More precisely, for  $\alpha = 1, 2$ , the component of the velocity  $u_\alpha$  is defined on the grid  $g_\alpha := g_0 - \frac{h}{2} \mathbf{e}_\alpha$ , where  $\mathbf{e}_\alpha$  is a unit vector in the  $\alpha$  direction. The pressure  $p$  and the diagonal elements  $A_{ii}$ 's of the extra stress tensor live on  $g_0$ , and the off-diagonal elements  $A_{ij}$ 's,  $i \neq j$ , are defined on the  $g_{-1} := g_0 - \frac{h}{2} \sum_\alpha \mathbf{e}_\alpha$ . A two-dimensional staggered MAC grid is illustrated in the right picture of Fig. 1.

Now we define two finite difference operators as follows:

$$(D_\alpha^{(1)} \phi)(\mathbf{x}) = \frac{\phi(\mathbf{x} + \frac{h}{2} \mathbf{e}_\alpha) - \phi(\mathbf{x} - \frac{h}{2} \mathbf{e}_\alpha)}{h}, \quad (18)$$

$$(D_\alpha^{(2)} \phi)(\mathbf{x}) = \frac{\phi(\mathbf{x} + h \mathbf{e}_\alpha) - \phi(\mathbf{x} - h \mathbf{e}_\alpha)}{2h}, \quad (19)$$

where  $\alpha = 1, 2$ . Note that these operators in  $\alpha$ th direction correspond to the partial derivatives of  $\phi(\mathbf{x})$  with respect to  $x_\alpha$ . Thus the discrete divergence and Laplace operators are defined by  $D_\beta^{(1)} u_\beta$  and  $L u_\alpha = D_\beta^{(1)} D_\beta^{(1)} u_\alpha$ , respectively, where we use the summation convention.

The fluid mesh and the immersed boundary mesh are connected by a smoothed approximation to the Dirac delta function. It is denoted  $\delta_h$  and is of the following form:

$$\delta_h(\mathbf{x}) = h^{-2} \psi\left(\frac{x_1}{h}\right) \psi\left(\frac{x_2}{h}\right), \quad (20)$$

where the function  $\psi$  is given by

$$\psi(r) = \begin{cases} \frac{3-2|r|+\sqrt{1+4|r|-4r^2}}{8}, & \text{if } |r| \leq 1 \\ \frac{5-2|r|-\sqrt{-7+12|r|-4r^2}}{8}, & \text{if } 1 < |r| \leq 2 \\ 0, & \text{if } 2 < |r|. \end{cases} \quad (21)$$

The motivation and derivation for this particular choice is discussed in [13].

With the help of the function  $\delta_h$ , we can interpolate a function  $\phi_\beta(\mathbf{x})$  defined only on  $\mathbf{x} \in g_\beta$  to be a function defined on  $\mathbf{y} \in g_\alpha$ . To be precise, we define the interpolation operator  $I_\alpha$  by

$$(I_\alpha \phi_\beta)(\mathbf{y}) = \sum_{\mathbf{x} \in g_\beta} \phi_\beta(\mathbf{x}) \delta_h(\mathbf{x} - \mathbf{y}) h^2, \quad (22)$$

where  $\mathbf{y} \in g_\alpha$ . Let  $S(\mathbf{u})\phi_\alpha$  denote the application of the discrete convective operator to a function  $\phi_\alpha$ , then it is the discretization of  $\frac{1}{2}((\mathbf{u} \cdot \nabla)\phi_\alpha + \nabla \cdot (\mathbf{u}\phi_\alpha))$ , and the explicit form of the skewsymmetric convective operator is

$$S(\mathbf{u})\phi_\alpha = \frac{1}{2} \sum_{\beta=1}^2 ((I_\alpha u_\beta) D_\beta^{(2)} \phi_\alpha + D_\beta^{(2)} ((I_\alpha u_\beta) \phi_\alpha)). \quad (23)$$

Note that the discrete functions used to define  $S(\mathbf{u})\phi_\alpha$  are all defined at points  $\mathbf{x} \in g_\alpha$ , and thus  $S(\mathbf{u})\phi_\alpha$  is a function of  $\mathbf{x} \in g_\alpha$ .

The  $\alpha\beta$  element of the deformation tensor  $\mathbf{d}(\mathbf{u}) = \frac{1}{2}(\nabla \mathbf{u} + (\nabla \mathbf{u})^T)$  can be discretized as

$$d_{\alpha\beta}(\mathbf{u}) = \frac{1}{2} (D_\alpha^{(1)} u_\beta + D_\beta^{(1)} u_\alpha). \quad (24)$$

We can see that  $(d_{\alpha\beta}(\mathbf{u}))(\mathbf{x})$  is a discrete function defined at the points  $\mathbf{x} \in g_0$  when  $\alpha = \beta$  and at the points  $\mathbf{x} \in g_{-1}$  when  $\alpha \neq \beta$ .

We also need to define the spatial discretization of the term  $\nabla \mathbf{u} \mathbf{A} + \mathbf{A}(\nabla \mathbf{u})^T$  in Eq. (3) of which the  $\alpha\beta$  element can be written as

$$\frac{\partial u_\alpha}{\partial x_\gamma} A_{\gamma\beta} + \frac{\partial u_\beta}{\partial x_\gamma} A_{\alpha\gamma}, \quad (25)$$

where we use the summation convention. The  $\alpha\beta$  element of the discretization of this operator, which we denote as  $C_{\alpha\beta}(\mathbf{u}, \mathbf{A})$ , can be defined as

$$C_{\alpha\beta}(\mathbf{u}, \mathbf{A}) = (D_\gamma^{(2)}(I_g u_\alpha))(I_g A_{\gamma\beta}) + (D_\gamma^{(2)}(I_g u_\beta))(I_g A_{\alpha\gamma}), \quad (26)$$

where  $g = 0$  when  $\alpha = \beta$ , and  $g = -1$  when  $\alpha \neq \beta$ . Thus  $C_{\alpha\beta}(\mathbf{u}, \mathbf{A})(\mathbf{x})$  is a discrete function defined at the points  $\mathbf{x} \in g_0$  when  $\alpha = \beta$  and at the points  $\mathbf{x} \in g_{-1}$  when  $\alpha \neq \beta$ .

### 3.2. Time-stepping scheme

The temporal iteration is based on the framework of a second-order Runge–Kutta method in which each time step is divided into two substeps: the preliminary substep to compute data at time level  $n + \frac{1}{2}$  using data at time level  $n$  and the final substep to update the data at time level  $n + 1$  using the data at time levels  $n$  and  $n + \frac{1}{2}$ . The step-by-step procedure of the time-stepping scheme proceeds as follows.

*Step 1:* Update the positions of the massless boundary  $\mathbf{X}_k^{n+\frac{1}{2}}$  and massive body  $\mathbf{Y}_{\text{cm}}^{n+\frac{1}{2}}$ .

$$\mathbf{X}_{k,\alpha}^{n+\frac{1}{2}} = \mathbf{X}_{k,\alpha}^n + \frac{\Delta t}{2} \sum_{\mathbf{x} \in g_\alpha} u_\alpha^n(\mathbf{x}) \delta_h(\mathbf{x} - \mathbf{X}_k^n) h^3, \quad \alpha = 1, 2, \quad (27)$$

$$\mathbf{Y}_{\text{cm}}^{n+\frac{1}{2}} = \mathbf{Y}_{\text{cm}}^n + \frac{\Delta t}{2} \mathbf{V}_{\text{cm}}^n, \quad (28)$$

$$\Omega^n = L^n / P_0, \quad (29)$$

$$\mathbf{E}_i^{n+\frac{1}{2}} = \mathcal{R} \left[ \frac{\Delta t}{2} \Omega^n \right] \mathbf{E}_i^n, \quad i = 1, 2, \quad (30)$$

$$\mathbf{Y}_k^{n+\frac{1}{2}} = \mathbf{Y}_{\text{cm}}^{n+\frac{1}{2}} + \mathcal{E}^{n+\frac{1}{2}} \mathbf{C}_k, \quad (31)$$

where  $\mathbf{V}_{\text{cm}}^n$  and  $L^n$  are the velocity of the center of mass and the angular momentum, respectively, which are known values at time  $n\Delta t$ , like  $\mathbf{u}^n$ .

*Step 2:* Calculate the force densities  $\mathbf{F}_k^{n+\frac{1}{2}}$  and  $\mathbf{f}^{n+\frac{1}{2}}$ , and the total torque  $\mathbf{T}^{n+\frac{1}{2}}$ .

$$\mathbf{F}_k^{n+\frac{1}{2}} = K \left( \mathbf{Y}_k^{n+\frac{1}{2}} - \mathbf{X}_k^{n+\frac{1}{2}} \right), \quad (32)$$

$$\mathbf{f}_\alpha^{n+\frac{1}{2}}(\mathbf{x}) = \sum_k \mathbf{F}_{k,\alpha}^{n+\frac{1}{2}} \delta_h \left( \mathbf{x} - \mathbf{X}_k^{n+\frac{1}{2}} \right) \Delta r \Delta s, \quad \alpha = 1, 2, \quad (33)$$

$$\mathbf{T}^{n+\frac{1}{2}} = \sum_k \left( \mathbf{Y}_k^{n+\frac{1}{2}} - \mathbf{Y}_{\text{cm}}^{n+\frac{1}{2}} \right) \times \left( -\mathbf{F}_k^{n+\frac{1}{2}} \right) \Delta r \Delta s. \quad (34)$$

Note that each component  $f_\alpha^{n+\frac{1}{2}}(\mathbf{x})$  of the force density  $\mathbf{f}^{n+\frac{1}{2}}$  is defined at  $\mathbf{x} \in g_\alpha$ .

*Step 3:* Given the computed force density  $\mathbf{f}^{n+\frac{1}{2}}$ , we solve the discretized version of the Oldroyd-B model (1)–(3) and compute the velocity  $\mathbf{V}_{\text{cm}}^{n+\frac{1}{2}}$  and the angular momentum  $L^{n+\frac{1}{2}}$ .

$$r_t \left( \frac{A_{\alpha\beta}^{n+\frac{1}{2}} - A_{\alpha\beta}^n}{\Delta t/2} + S(\mathbf{u}^n) A_{\alpha\beta}^n - C_{\alpha\beta}(\mathbf{u}^n, \mathbf{A}^n) \right) + A_{\alpha\beta}^{n+\frac{1}{2}} = 2\mu_p d_{\alpha\beta}(\mathbf{u}^n), \quad (35)$$

$$\rho \left( \frac{u_\alpha^{n+\frac{1}{2}} - u_\alpha^n}{\Delta t/2} + S(\mathbf{u}^n)u_\alpha^n \right) + D_\alpha^{(1)} p^{n+\frac{1}{2}} = \mu_s L u_\alpha^{n+\frac{1}{2}} + D_\gamma^{(1)} A_{\alpha\gamma}^{n+\frac{1}{2}} + f_\alpha^{n+\frac{1}{2}}, \quad (36)$$

$$D_\gamma^{(1)} u_\gamma^{n+\frac{1}{2}} = 0 \quad (37)$$

$$\mathbf{V}_{\text{cm}}^{n+\frac{1}{2}} = \mathbf{V}_{\text{cm}}^n + \frac{\Delta t}{2M} \sum_k (-\mathbf{F}_k^{n+\frac{1}{2}}) \Delta r \Delta s - \frac{\Delta t}{2} g \mathbf{e}_2. \quad (38)$$

$$L^{n+\frac{1}{2}} = L^n + \frac{\Delta t}{2} T^{n+\frac{1}{2}}, \quad (39)$$

where  $\alpha, \beta = 1, 2$ . Eq. (35) is defined for  $\mathbf{x} \in g_0$  when  $\alpha = \beta$  and  $\mathbf{x} \in g_{-1}$  when  $\alpha \neq \beta$ . Eqs. (36) and (37) hold for  $\mathbf{x} \in g_\alpha$  and  $\mathbf{x} \in g_0$ , respectively.

**Step 4:** Update the massless boundary  $\mathbf{X}_k^{n+1}$  and massive body body  $\mathbf{Y}_k^{n+1}$ .

$$X_{k,\alpha}^{n+1} = X_{k,\alpha}^n + \Delta t \sum_{\mathbf{x} \in g_\alpha} u_\alpha^{n+\frac{1}{2}}(\mathbf{x}) \delta_h(\mathbf{x} - \mathbf{X}_k^{n+\frac{1}{2}}) h^2, \quad \alpha = 1, 2, \quad (40)$$

$$\mathbf{Y}_{\text{cm}}^{n+1} = \mathbf{Y}_{\text{cm}}^n + \Delta t \mathbf{V}_{\text{cm}}^{n+\frac{1}{2}}, \quad (41)$$

$$\Omega^{n+\frac{1}{2}} = L^{n+\frac{1}{2}} / P_0 \quad (42)$$

$$\mathbf{E}_i^{n+1} = \mathcal{R}[\Delta t \Omega^{n+\frac{1}{2}}] \mathbf{E}_i^n, \quad i = 1, 2, \quad (43)$$

$$\mathbf{Y}_k^{n+1} = \mathbf{Y}_{\text{cm}}^{n+1} + \mathcal{E}^{n+1} \mathbf{C}_k. \quad (44)$$

**Step 5.** Update the fluid velocity, the velocity of the center of mass, and the angular momentum of the rigid body: for  $\alpha, \beta = 1, 2$ ,

$$\begin{aligned} r_t \left( \frac{A_{\alpha\beta}^{n+1} - A_{\alpha\beta}^n}{\Delta t} + S(\mathbf{u}^{n+\frac{1}{2}}) A_{\alpha\beta}^{n+\frac{1}{2}} - C_{\alpha\beta}(\mathbf{u}^{n+\frac{1}{2}}, \mathbf{A}^{n+\frac{1}{2}}) \right) + A_{\alpha\beta}^{n+1} \\ = 2\mu_p d_{\alpha\beta}(\mathbf{u}^{n+\frac{1}{2}}), \end{aligned} \quad (45)$$

$$\begin{aligned} \rho \left( \frac{u_\alpha^{n+1} - u_\alpha^n}{\Delta t} + S(\mathbf{u}^{n+\frac{1}{2}}) u_\alpha^{n+\frac{1}{2}} \right) + D_\alpha^{(1)} p^{n+1} \\ = \frac{1}{2} \mu_s L (u_\alpha^{n+1} + u_\alpha^n) + \frac{1}{2} D_\gamma^{(1)} (A_{\alpha\gamma}^{n+1} + A_{\alpha\gamma}^n) + f_\alpha^{n+\frac{1}{2}}, \end{aligned} \quad (46)$$

$$D_\gamma^{(1)} u_\gamma^{n+1} = 0 \quad (47)$$

$$\mathbf{V}_{\text{cm}}^{n+1} = \mathbf{V}_{\text{cm}}^n + \frac{\Delta t}{M} \sum_{k=1}^N (-\mathbf{F}_k^{n+\frac{1}{2}}) \Delta r \Delta s - \Delta t g \mathbf{e}_2. \quad (48)$$

$$L^{n+1} = L^n + \Delta t T^{n+\frac{1}{2}}. \quad (49)$$

This completes the time-stepping scheme.

### 3.3. Implementation of fixed walls

In order to solve the Oldroyd-B Eqs. (35)–(37) and (45)–(47), we use the assumption of periodic boundary conditions and adopt the discrete Fourier transform (implemented by the FFT algorithm). This is because the fluid equations can be solved efficiently by using the FFT algorithm. (Note, however, that there is no fundamental restriction on the fluid solver and the boundary conditions in the present method.) Though we use periodic boundary conditions in all two space directions for computational efficiency, we can break the periodicity and make fixed walls.

In order to model fixed walls, we utilize the “target boundary” idea. We designate target boundary points  $\mathbf{W}_0(s)$  in the place where we want the internal walls to be. To avoid fluid leakage through the wall, the

target boundary points should be spaced about half a mesh width apart (or closer). The target boundary points neither move nor interact with the fluid directly, but they are connected by a system of stiff springs to the immersed boundary points  $\mathbf{W}(s, t)$  that move at the local fluid velocity and apply force locally to the fluid, see the left picture of Fig. 1. When the wall boundary  $\mathbf{W}(s, t)$  moves apart from the target boundary  $\mathbf{W}_0(s)$ , a restoring force comes into play to keep them as close to each other as possible. The restoring force  $\mathbf{F}_w(s, t)$  acting on the wall boundary  $\mathbf{W}(s, t)$  is defined as

$$\mathbf{F}_w(s, t) = K_w (\mathbf{W}_0(s) - \mathbf{W}(s, t)), \quad (50)$$

where  $K_w$  is a large stiffness constant. This provides a feedback mechanism for computing the boundary force needed to force the immersed boundary to stay in the stationary internal walls. Note that the target boundary idea for enforcing the no-slip condition still allows the use of FFT, since we do so not by changing the boundary conditions per se but instead by applying forces that effectively prevent the fluid from moving at the specified locations. This idea has been successfully used to simulate a stationary boundary in many previous works [27–29].

## 4. Numerical results

We verify the present pIB method for viscoelastic particulate flows by simulating some simple systems. First, we simulate a circular particle falling under the influence of gravity in 2D space and compute the following dimensionless parameters:

$$\text{Reynolds number, } \text{Re} = \rho U D / (\mu_s + \mu_p), \quad (51)$$

$$\text{Deborah number, } \text{De} = U r_t / D, \quad (52)$$

$$\text{drag coefficient, } C_D = \frac{\pi(D/2)^2 (\rho_L - \rho) g}{\frac{1}{2} \rho U D}, \quad (53)$$

where  $U$  is the terminal descent velocity and  $D$  is the diameter of the particle.

We then validate the present method further by a convergence study, which shows that it is first-order accurate. Although we use second-order accurate discretizations in space and time, the method of this paper is only first-order accurate spatially, since it is applied to problems of which solutions lack sufficient spatial smoothness for the formal second-order accuracy of the method to be realized in practice. Next, we consider two circular particles which simultaneously descend in a channel filled with an Oldroyd-B fluid. The simulation results will be compared with those in the literature. Finally, we simulate the sedimentation of several particles in a viscoelastic fluid.

In the traditional IB (pIB) method, it is conventional that the distance between two neighboring marker points should be approximately less than half a meshwidth. Throughout this section, we distribute the mass uniformly over the rigid circular particle with the grid spacing being  $\Delta r$  in the  $x$  direction and  $\Delta s$  in the  $y$  direction, which both are less than  $h/2$ , and thus the center of mass is the geometrical center of the rigid body. See the upper-left panel of Fig. 2 which shows a schematic view for the marker points (“+”) representing the circular particle. Note, however, that mass could be distributed non-uniformly, which would affect the moment of inertia.

### 4.1. A falling circular particle and convergence study

We begin by investigating the case of a single circular particle falling in a channel filled with an Oldroyd-B fluid with  $\rho = 1.0 \text{ g/cm}^3$ ,  $r_t = 1.0 \text{ s}$ ,  $\mu_s = 0.05 \text{ g/(cm} \cdot \text{s)}$ , and  $\mu_p = 0.15 \text{ g/(cm} \cdot \text{s)}$ . We choose a computational domain  $[-0.75, 0.75] \times [0, 6] \text{ cm}^2$ ; however, the channel width is  $1.0 \text{ cm}$  by setting up two vertical walls at  $x = -0.5 \text{ cm}$  and  $x = 0.5 \text{ cm}$ . The particle diameter and density are  $D = 0.25 \text{ cm}$  and  $\rho_L = 1.01 \text{ g/cm}^3$  (thus the excess mass density  $m = 0.01 \text{ g/cm}^3$ ), respectively, and the gravity with

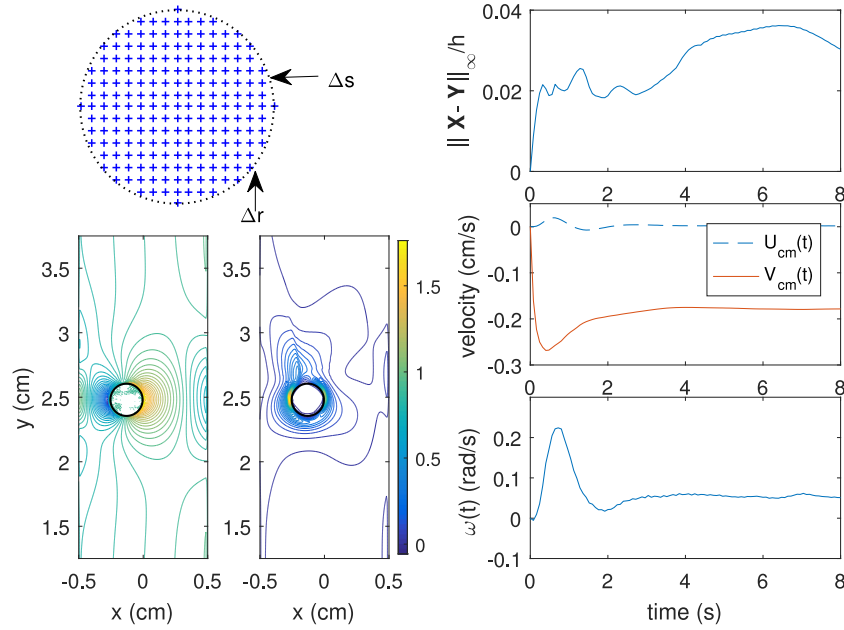


**Fig. 2.** The upper-left shows a schematic view for the marker points ('+') representing the circular particle with the grid spacings  $\Delta r$  and  $\Delta s$ . The two lower-left panels show the vorticity contours (1st column) of flow past a freely falling circular particle and the trace contours (2nd column) of the extra stress tensor  $\mathbf{A}$  at  $t = 8$  s. The upper right panel, which plots the maximum distance between the two descriptions of the particle, shows that  $\|\mathbf{X} - \mathbf{Y}\|_\infty$  is less than  $h/25$ . The right-middle and right-bottom panels show the  $x$  and  $y$  components of velocity  $\mathbf{V}_{cm}(t)$  and the angular velocity  $\omega(t)$ , respectively.

$g = 980 \text{ cm/s}^2$  acts in the negative  $y$ -direction. The simulation begins at  $t = 0$  by releasing the particle at the initial position  $(-0.15 \text{ cm}, 4.0 \text{ cm})$ . The meshwidth is  $h = 1.5/256 \text{ cm}$ , and the time step is  $\Delta t = 10^{-5} \text{ s}$ . This case is identical to the one presented in [7] except that we here use periodic boundary conditions for the fluid equations instead of Dirichlet boundary conditions used in [7].

The 1st column of Fig. 2 shows vorticity contours at  $t = 8 \text{ s}$  for the freely falling particle in the Oldroyd-B fluid from which we can see the counter vortices in the left and right sides of the particle. The 2nd column depicts the trace contours of the extra stress tensor  $\mathbf{A}$  at  $t = 8 \text{ s}$  which is used to show the distribution of normal stress. We can see that the trace of the extra stress tensor is large around the particle with its maximum at the left and right sides of the particle and decreases to be 0 as we go far away from the particle.

The present pIB method uses the penalty parameter  $K$  which forces the two descriptions of the body to be close to each other. A large  $K$  causes a large force for any given displacement and may then lead to a computational instability which can be avoided by reducing the time step  $\Delta t$ . We choose the parameter  $K$  to ensure the distance between the two Lagrangian descriptions to be less than one-tenth the meshwidth, i.e.,  $\|\mathbf{X} - \mathbf{Y}\|_\infty \leq h/10$ , and adjust the time step  $\Delta t$  to avoid numerical instability for a large  $K$ . This can be achieved here by setting  $K = 2.56 \times 10^8 \text{ g/(cm}^4\text{s}^2)$  and  $\Delta t = 10^{-5} \text{ s}$ . The upper right panel of Fig. 2, which plots the maximum distance between the two descriptions  $\mathbf{X}$  and  $\mathbf{Y}$  of the particle, shows that  $\|\mathbf{X} - \mathbf{Y}\|_\infty$  is less than  $h/25$ .

The two lower-right panels of Fig. 2 show the time evolution of the  $x$  and  $y$  components of the velocity  $\mathbf{V}_{cm}(t)$  (middle) of the particle and the angular velocity  $\omega(t)$  (bottom), respectively. The body accelerates downwards until it reaches its steady descent velocity around at  $t = 3.0 \text{ s}$ , called the terminal velocity. After reaching the terminal velocity, the body falls with an approximately constant velocity  $V_{cm} = -0.179 \text{ cm/s}$  which leads  $\text{Re} = 0.2244$ ,  $\text{De} = 0.716$ , and  $C_D = 21.506$ . These values are comparable to the data in [7]. A large overshoot of the descent velocity and the angular velocity, followed by steady velocities, can be observed in the figure, which is consistent with other observations [6–8]. We can also see from the right-bottom panel that the particle rotates counter-clockwise which indicates the rolling of the particle near wall [5,7].

We now perform a convergence study to verify that the rigid body dynamics in an Oldroyd-B fluid is correctly solved by the present pIB method. Here we vary the mesh sizes of the  $x$  and  $y$  directions of the domain as  $(N_x, N_y) = (64, 256)$ ,  $(128, 512)$ ,  $(256, 1024)$ , and  $(512, 2048)$  so that the mesh width becomes  $h = 1.5/N_x$  correspondingly. We also choose  $\Delta r = \Delta s = 0.64/N_x$  and  $\Delta t = 2.56 \cdot 10^{-3}/N_x$  which are proportional to  $h$ , so that the refinements for the fluid mesh width, the boundary mesh width, and the time step duration are done by the same factor, see the upper-left panel of Fig. 2. When we refine the mesh width and time step, we increase the penalty parameter as  $K = 3.90625 \times 10^3 N_x^2 \text{ g/(cm}^4\text{s}^2)$ . Note that the penalty parameter  $K$  increases as timestep is refined in the manner that  $K\Delta t^2$  is constant. The fact that this relationship between  $K$  and  $\Delta t$  preserves the numerical stability of the scheme despite the increase of  $K$  was proved by Lai [30].

The left panel of Fig. 3 shows the descent velocity  $V_{cm}(t)$  as functions of time for the four  $N_x$ 's. We can see that the velocities are close for the four cases of  $N_x$ . Especially, the difference of the descent velocities between the cases of  $N_x = 256$  and 512 is smaller than those between the cases of other pairs with coarser resolutions, which might imply the convergence behavior of the solutions.

To get a more quantitative measure of convergence, we compare the velocity fields computed on the four different mesh widths. Since we do not have the exact solution for the problem, the estimation of the convergence ratio requires three numerical solutions for three consecutive grid sizes  $N_x$ 's. We first define the discrete  $L_2$  norm of a scalar valued function  $\psi$  defined on the Cartesian grid as  $\|\psi\|_2 = (\sum_{i,j} |\psi_{i,j}|^2 h^2)^{1/2}$ . Let  $(u_{N_x}, v_{N_x})$  be the velocity field for  $N_x \times N_y$  Cartesian grid, then the right panel of Fig. 3 shows the convergence ratios of the computed fluid velocity which is computed by  $(\|u_{N_x} - u_{2N_x}\|_2^2 + \|v_{N_x} - v_{2N_x}\|_2^2)^{1/2} / (\|u_{2N_x} - u_{4N_x}\|_2^2 + \|v_{2N_x} - v_{4N_x}\|_2^2)^{1/2}$  for each of the cases  $N_x = 64$  (dashed line) and 128 (solid line). One can see from the figure that the convergence ratios for the fluid velocity are around 2, which indicates that the present method is first-order accurate. As remarked above, the IB method is typically first-order accurate, despite its formal second-order accuracy. There are some special situations in which actual second-order accuracy is achieved [16], but these seem to be those that avoid a delta-function layer of force at the solid-fluid interface. Such a delta-function layer is

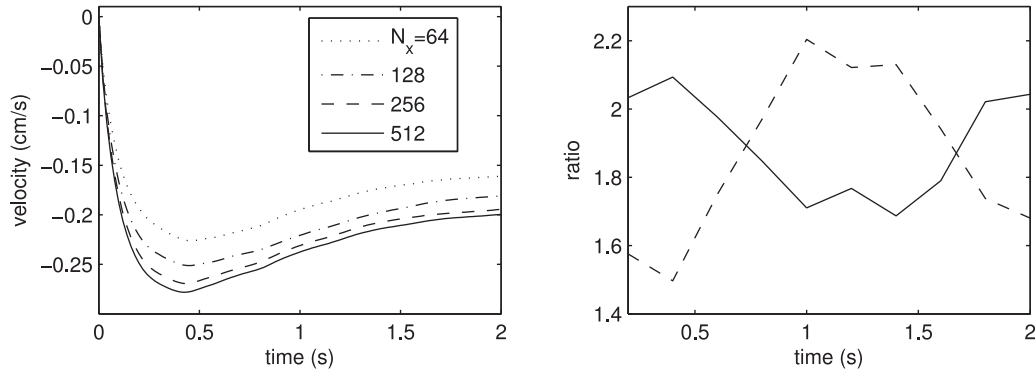


Fig. 3. The left panel shows the descent velocity  $V_{cm}(t)$  for the four  $N_x$ 's, and the right panel shows the convergence ratios (defined in the text) of the computed velocity field  $\mathbf{u}(\mathbf{x}, t)$  for  $N_x = 64$  (dashed line) and 128 (solid line). The descent velocities are very close for the four  $N_x$ 's, and the convergence ratios for the velocity are near 2 (first-order accuracy).

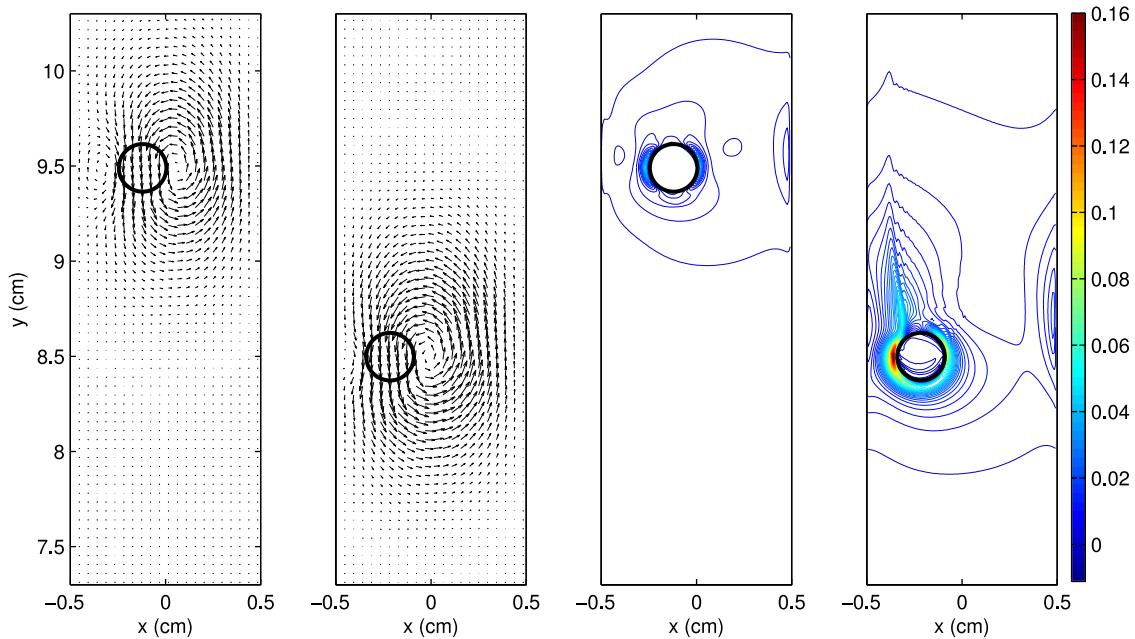


Fig. 4. Velocity fields (left two columns) and traces of the extra stress tensor  $\mathbf{A}$  (right two columns) at time  $t = 96$  s in the cases with two different relaxation times:  $r_t = 1.0$  s (1st and 3rd columns) and 4.0 s (2nd and 4th columns).

needed here, despite the thickness of the solid, to enforce the no-slip condition at a rigid boundary.

#### 4.2. Elasticity effect on a falling circular particle

We here vary the relaxation time  $r_t$  to investigate the effect of elasticity on the lateral equilibrium position. The elastic effect is measured by the elasticity number  $E = De/Re$ . The parameters are chosen as  $\rho = 1.0 \text{ g/cm}^3$ ,  $\mu_s = 0.00425 \text{ g/(cm}\cdot\text{s)}$ , and  $\mu_p = 0.02975 \text{ g/(cm}\cdot\text{s)}$ . The particle, which has the diameter  $D = 0.25 \text{ cm}$  and density  $\rho_L = 1.0007 \text{ g/cm}^3$ , is released at the initial position  $(-0.15 \text{ cm}, 15.0 \text{ cm})$  in the rectangular domain  $[-0.5, 0.5] \times [0, 16] \text{ cm}^2$ .

Fig. 4 draws the velocity fields (left two columns) and the traces of the extra tensor  $\mathbf{A}$  (right two columns), at time  $t = 96$  s when the particles reach their terminal velocity. The figure compares two cases with two different relaxation times:  $r_t = 1.0$  s (1st and 3rd columns) and 4.0 s (2nd and 4th columns). While the velocity field with  $r_t = 1.0$  s has two counter-rotating vortices around the particle, the velocity field with  $r_t = 4.0$  s has only one at the right of the particle. This is because the particle in the latter case is too close to the left wall for the flow to form a vortex at the right side. The trace of  $\mathbf{A}$  is positive around the

particle with its maximum on the sides of the particle in both cases. We can also see that the magnitude of the trace and the region of positive trace are larger in the flow with a larger relaxation time (compare the right two columns).

We also investigate the effects of the elasticity and wall by releasing the particle at different distances from the wall. We choose the same parameters used in the previous simulations and also in [7]; however, the relaxation time  $r_t$  is chosen as 0, 1.0 s, 2.0 s, 4.0 s, 8.0 s, and 16.0 s, and the particle is released from two different lateral positions  $x = -0.15 \text{ cm}$  and  $-0.25 \text{ cm}$ . Note that, when  $r_t = 0$ , the fluid is Newtonian, and we use the fluid viscosity to be  $\mu_s + \mu_p = 0.00425 + 0.02975 = 0.034 \text{ g/(cm}\cdot\text{s)}$ .

The upper panel of Fig. 5 shows the descent velocity of the particle released at  $x = -0.15 \text{ cm}$  in terms of time. Two different time scales are used in the  $x$ -axis to see more clearly the initial behaviors of the particles. The overshoot of the descent velocity gets smaller as the relaxation time gets smaller and disappears when the flow is Newtonian as shown in the upper-left panel. Independent of the relaxation time and the initial overshoot, all the flows reach their terminal velocities which are inversely proportional to the relaxation time  $r_t$  when  $r_t \leq 4.0$  s; however, the terminal velocity decreases as the relaxation time increases when  $r_t \geq 4.0$  s. (Compare the terminal velocities for  $r_t = 4.0$  s,

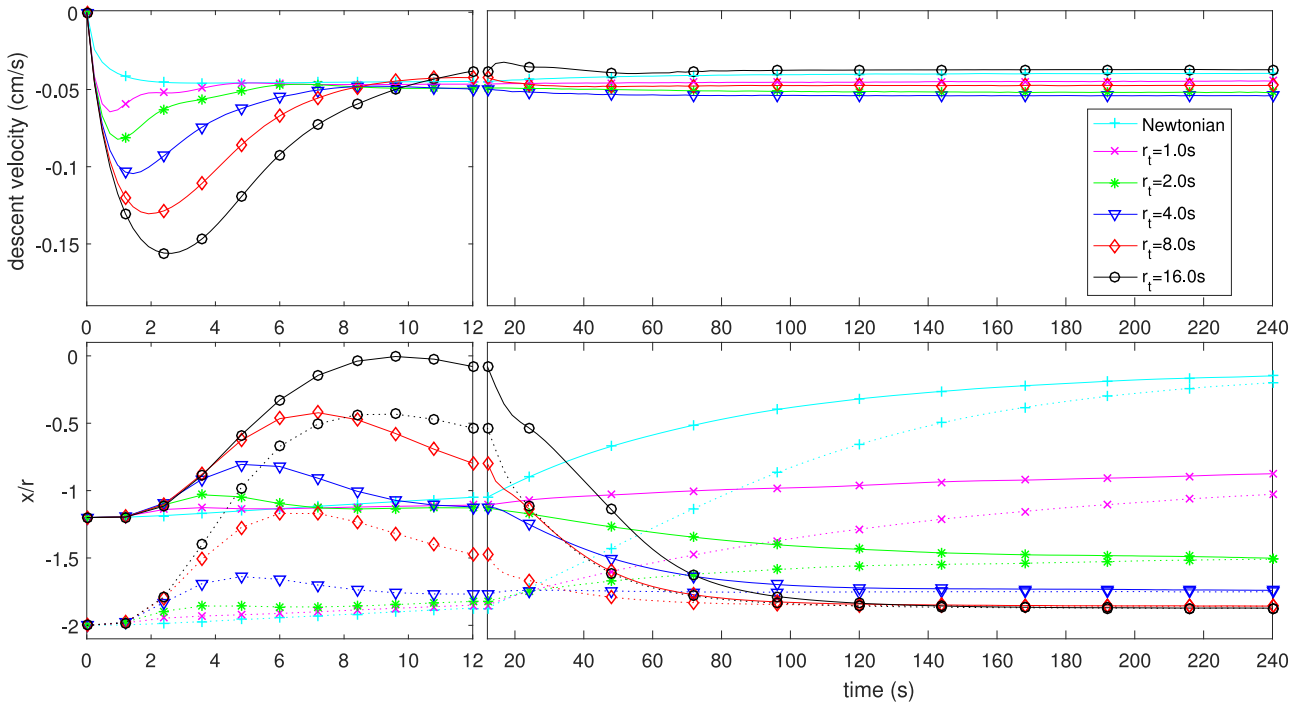


Fig. 5. The descent velocity of the particle released at  $x = -0.15$  cm as functions of time (upper) and the lateral position of the particle normalized by the particle radius  $r$  (lower) which is released at  $x = -0.15$  cm (solid lines) and  $x = -0.25$  cm (dotted lines). The initial time scale (left) is larger than the later one (right). Independent of the initial released position, there exists a lateral equilibrium position which depends only on the relaxation time and which is closer to the wall as the relaxation time  $r_t$  gets larger.

Table 1

Reynolds, Deborah, elasticity numbers, drag coefficients, and the lateral equilibrium position of the center of mass.

$r_t$	0	1.0 s	2.0 s	4.0 s	8.0 s	16.0 s
Re	0.291	0.328	0.381	0.397	0.348	0.273
De	0	0.178	0.415	0.864	1.516	2.374
E	0	0.554	1.088	2.176	4.352	8.704
$C_D$	6.80	6.046	5.196	4.99	5.687	7.261
Lateral position	0	$-0.883 r$	$-1.495 r$	$-1.739 r$	$-1.857 r$	$-1.872 r$

8.0 s, and 16.0 s.) Table 1 shows the induced steady non-dimensional quantities for each of the relaxation times. As the relaxation time  $r_t$  increases, Deborah (De) and elasticity (E) numbers increase. While the Reynolds number (Re) increases up to  $r_t = 4.0$  s and then decreases as the relaxation time  $r_t$  increases, the drag coefficient ( $C_D$ ) has the opposite behavior.

The lower panel of Fig. 5 shows the lateral position of the center of mass  $Y_{cm}(t)$  of the particles normalized by the particle radius  $r$ . The lines with the same markers (or same color) represent an Oldroyd-B fluid with the same relaxation time. The pair of lines with the same markers represents two different initial lateral positions:  $x = -0.15$  cm (solid line) and  $-0.25$  cm (dotted line). Each pair of lines with the same markers goes to the same lateral position, i.e., the particles in the fluid with the same relaxation time reach almost the same lateral equilibrium position independent of the initial lateral position. We can also observe some initial overshoot of the lateral position when  $r_t \geq 2.0$  s, i.e., the particle is pushed away from the wall initially, then attracted to drift toward the wall again, and gradually approach the eccentric equilibrium position [7]. The initial overshoot of the lateral position gets larger as the relaxation time  $r_t$  gets larger.

The lateral equilibrium position depends only on the relaxation time and gets closer to the wall as the relaxation time  $r_t$  (and thus elasticity number E) gets larger, see also Table 1. These behaviors are also in good

agreement with the ones observed in [7,8,31]. However, we find that the lateral equilibrium position has a limit even though the relaxation time further increases. When  $r_t = 8.0$  s and 16.0 s, Table 1 shows that the two lateral equilibrium positions are  $-1.857 r$  and  $-1.872 r$ , respectively. The lateral equilibrium positions for larger relaxation times are found to be very close to these values: in particular,  $-1.859 r$  for  $r_t = 20.0$  s and  $-1.834 r$  for  $r_t = 24.0$  s.

It is interesting to see from Table 1 that, as we increase the relaxation time  $r_t$ , the drag first decreases and then increases. Especially, the drag coefficient is largest at  $r_t = 16.0$  s. The reason for this might be that the particle in the case with  $r_t = 16.0$  s is so close to the wall that the velocity gradient close to the particle surface and, accordingly, the shear stress (and thus the drag) on the particle surface increase [32,33]. The gap between the wall and the particle is only  $1.128 r$  at  $r_t = 16.0$  s.

### 4.3. Sedimentation of multiple circular particles

In this subsection, we investigate the interaction between multiple circular particles falling freely in a steady fluid. Throughout this section, we choose a computational domain  $[-0.5, 0.5] \times [0, 16]$  cm<sup>2</sup> filled with an Oldroyd-B fluid. As the first test case, we release two identical particles which have diameter  $D = 0.125$  cm and density  $\rho_L = 1.01$  g/cm<sup>3</sup> at the initial positions  $(-0.15$  cm, 13.0 cm) and  $(0.15$  cm, 13.001 cm). The Oldroyd-B fluid has the following properties:  $\rho = 1.0$  g/cm<sup>3</sup>,  $r_t = 1.0$  s,  $\mu_s = 0.05$  g/(cm·s), and  $\mu_p = .15$  g/(cm·s). The meshwidth is  $h = 1/128$  cm, the time step is  $\Delta t = 1.6 \times 10^{-5}$  s, and the final time is 128 s.

The left two columns of Fig. 6 show the motion of the falling particles in a Newtonian fluid (1st column) and in the Oldroyd-B fluid with  $r_t = 1.0$  s (2nd column) at the selected times:  $t = 12.8$  s, 25.6 s, 38.4 s, 51.2 s, 64.0 s, 76.8 s, 89.6 s, and 102.4 s. The Newtonian fluid has the viscosity  $\mu_s + \mu_p = 0.05 + 0.15 = 0.2$  g/(cm·s). We can see from the 2nd column that the two particles undergo drafting until kissing, tumbling of the combined particles until they are aligned with the falling direction,

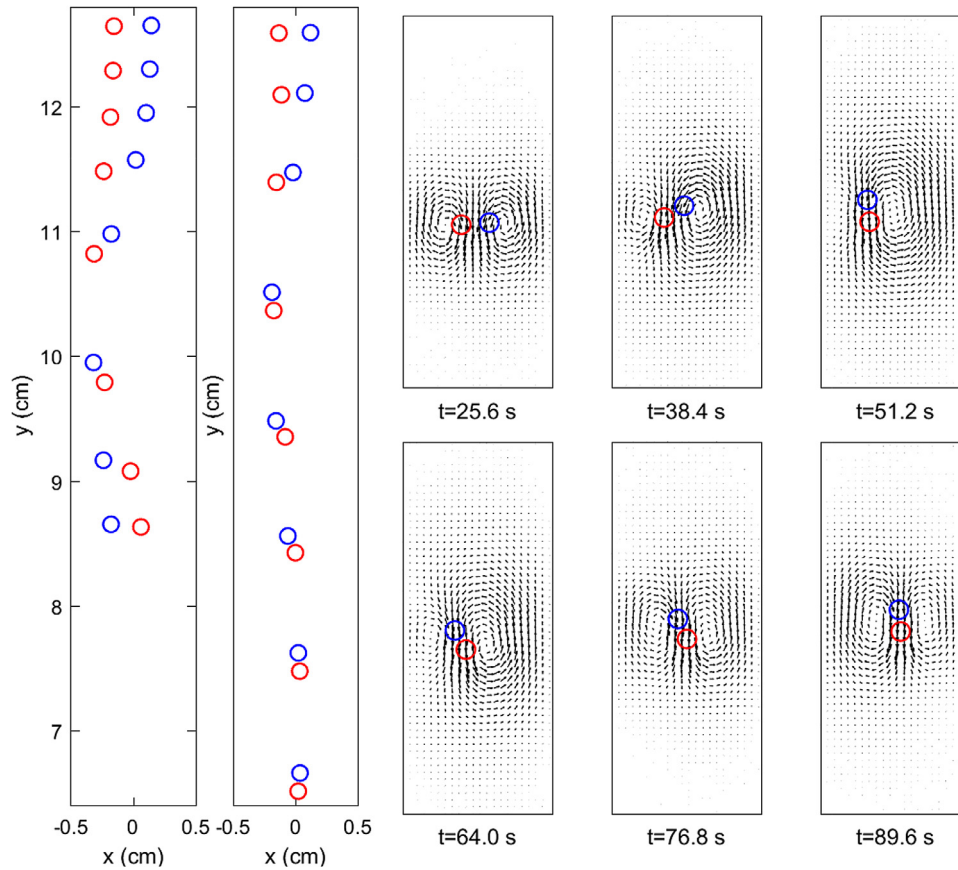


Fig. 6. The left two panels compare the interaction between two descending particles in the Newtonian fluid (1st column) and in the Oldroyd-B fluid with  $r_t = 1.0$  s (2nd column) at the selected times:  $t = 12.8$  s, 25.6 s, 38.4 s, 51.2 s, 64.0 s, 76.8 s, 89.6 s, and 102.4 s. The right six panels show the snapshots of the doublet at several times, showing the phenomenon of drafting, kissing, tumbling, and chaining for two particles in the Oldroyd-B fluid.

and descending without separation. This is a well known behavior of two descending circular particles in an Oldroyd-B fluid [5,6,12]. Unlike these interactions of two particles in a non-Newtonian fluid, the particles in a Newtonian fluid go through a slow drafting, tumbling without kissing, and separation again. Note that the particles attract, kiss, and chain only when the relaxation time is larger than a critical value. When we simulate the interaction of two particles in the Oldroyd-B fluid with  $r_t = 0.1$  s (not shown here), they behave as in a Newtonian fluid.

The right six panels of Fig. 6 show the snapshots of the doublet at various moments of time, showing the phenomenon of drafting, kissing, and chaining for two particles in the viscoelastic fluid. Although the two particles (and generally multiple particles) can collide, it is important to note that no special method to detect and prevent collision was required during the computation. Non-penetration of immersed bodies  $\mathbf{X}(r, s, t)$  is an automatic feature of the IB method and follows (if the time step is sufficiently small) from the continuity of the interpolated velocity field in which the immersed bodies move. Indeed, when collisions seem to occur in an IB computation, there is always a small gap that remains between the colliding bodies. The gap size is of the same order of magnitude as the meshwidth  $h$  of the fluid computation.

To see more quantitatively the chaining behavior of the two particles in the Oldroyd-B fluid, we draw Fig. 7 in which the upper panels depict the time evolution of the  $x$  (left) and  $y$  (right) components of the centers  $\mathbf{Y}_{\text{cm}}(t)$  of the two particles, and the lower panels show their descent (left) and angular (right) velocities,  $V_{\text{cm}}(t)$  and  $\omega(t)$ . We can see from the upper panels that the chain of the two particles is formed at around  $t = 40$  s and descends approximately on the centerline of the domain. After around  $t = 90$  s, the angular velocity  $\omega(t)$  becomes almost 0, and the descent velocity  $V_{\text{cm}}(t)$  converges approximately to a constant value.

The average terminal velocity of the chain is  $-0.0746$  cm/s with the Reynolds number  $\text{Re} = 0.0467$ , Deborah number  $\text{De} = 0.597$ , and the elasticity number  $E = 12.8$ .

When the chain of two particles fall, they are aligned with the falling direction at the centerline of the domain in the Oldroyd-B fluid with  $r_t = 1.0$  s, as shown in the 2nd column of Fig. 6. We find, however, that, when the relaxation time gets larger, the combined particles fall with some tilt angle from the falling direction, and the lateral position of the particles moves to the wall. See the left panel of Fig. 8 in which we draw two descending particles in the Oldroyd-B fluid with  $r_t = 4.0$  s at various times:  $t = 38.4$  s, 51.0 s, 64.0 s, and 76.8 s. We can see that the lateral equilibrium position of the combined particles exists off the centerline of the domain and that the angle  $\theta$  between the line connecting the two particles and the positive  $y$ -axis is non-zero.

The upper-right panel of Fig. 8 shows the average value of the lateral positions of the two particles as functions of time for various relaxation times. When the relaxation time is small ( $r_t = 1.0$  s or 2.0 s), the lateral position of the combined particles converges to the centerline of the domain; however, as the relaxation time  $r_t$  gets larger over  $r_t = 2.0$  s, the lateral equilibrium position gets closer to the wall. This is a reminiscence of the effect of the elasticity on the lateral equilibrium position of a single descending particle in Section 4.2.

The lower-right panel of Fig. 8 shows the angle  $\theta$  between the line connecting the two particles and the positive  $y$ -axis as functions of time for various relaxation times. The angle  $\theta$  is drawn after  $t = 45.0$  s when the two particles are chained. When the relaxation time is small ( $r_t = 1.0$  s or 2.0 s), the tilt angle  $\theta$  oscillates and converges to 0, i.e., the particles are aligned with the falling direction. When the relaxation time is larger than 2.0 s, the tilt angles stay at some positive values which depend on

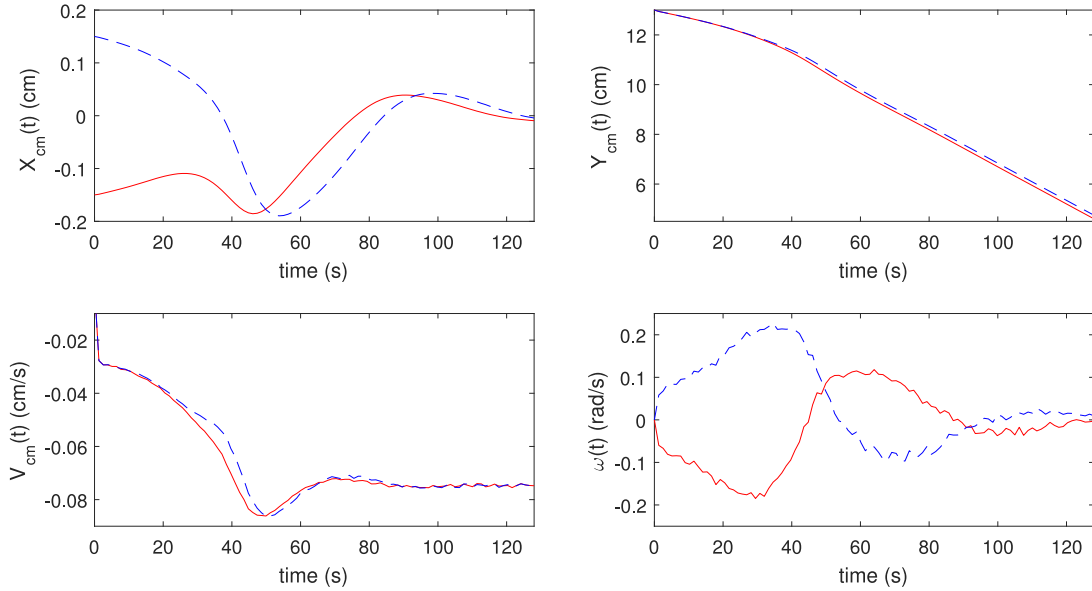


**Fig. 7.** The horizontal and vertical positions of the centers of mass (upper panels), the vertical velocities of the centers of mass (lower-left), and the angular velocities of rotation of the two particles about their centers of mass (lower-right). In the plots, the solid red lines and the dashed blue lines refer to the initially left and right particles, respectively, see Fig. 6. (For interpretation of the references to color in this figure legend, the reader is referred to the web version of this article.)

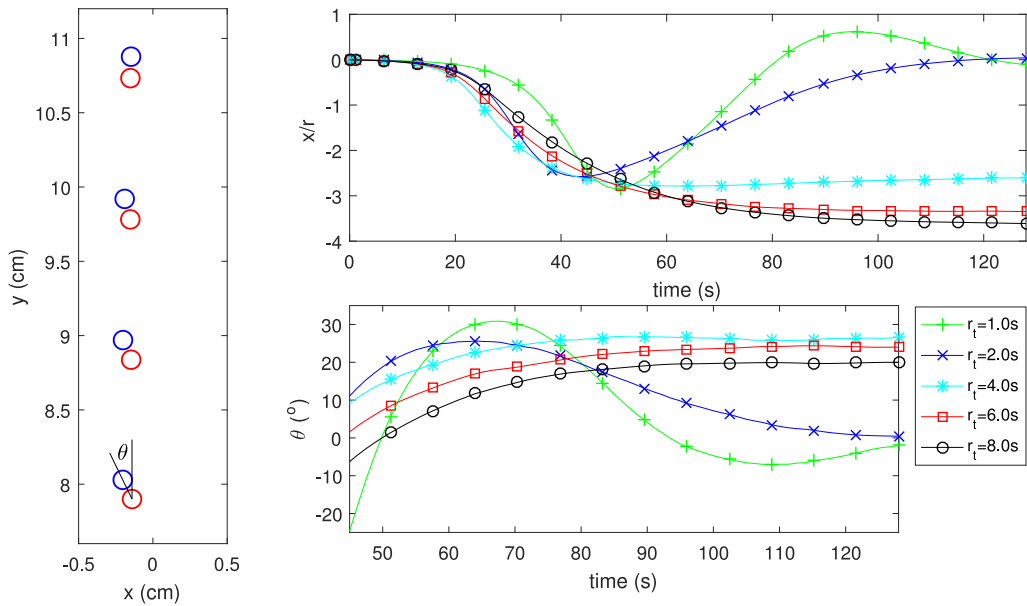


**Fig. 8.** The interaction between two particles falling in Oldroyd-B fluid with  $r_t = 4.0$  s at some chosen times (left), the average value of the lateral positions of the two particles as functions of time (upper-right), and the angle  $\theta$  between the line connecting the two particles and the positive  $y$ -axis as functions of time for various relaxation times. When  $r_t > 2.0$  s, the tilt angles stay at some positive values which depend on the relaxation time, and the lateral equilibrium position gets closer to the wall as the relaxation time gets larger.

the relaxation time  $r_t$ , see the graphs for  $r_t = 4.0$  s, 6.0 s, and 8.0 s. This result is a reminiscence of the recent observations that there exists an equilibrium tilt angle of a single ellipse or ellipsoid falling in a channel which is determined through the competition between inertia force and normal stress [3,34]. The dependence of tilt angle of two chained particles on elasticity and Mach numbers was also investigated in [35].

The next test case concerns three circular particles sedimenting in a channel filled with an Oldroyd-B fluid which has the following properties:  $\rho = 1.0$  g/cm<sup>3</sup>,  $\mu_s = 0.0325$  g/(cm · s),  $\mu_p = 0.2275$  g/(cm · s), and two different relaxation times  $r_t = 1.5$  s and 3.0 s. Then three particles, which are identical and have diameter  $D = 0.2$  cm and density  $\rho_L = 1.005$  g/cm<sup>3</sup>, are released at the initial positions  $(-0.3$  cm,

15.0 cm),  $(-0.02$  cm, 15.0 cm), and  $(0.26$  cm, 15.0 cm). The meshwidth is  $h = 1/128$  cm, the time step is  $\Delta t = 3.2 \times 10^{-5}$  s, and the final time is 160 s.

Fig. 9 compares the interaction of the three particles in a Newtonian fluid (upper panels) and Oldroyd-B fluids with the relaxation time  $r_t = 1.5$  s (middle panels) and 3.0 s (lower panels). We can see that the three particles form a chain along the falling direction only in the Oldroyd-B fluids, which verifies the well-known observations and experiments [7]. Whereas the chain is preserved in the Oldroyd-B fluid with a high relaxation time ( $r_t = 3.0$  s, lower panels), one of three particles breaks the chain to get far away from the chain of the other two particles in the Oldroyd-B fluid with a low relaxation time ( $r_t = 1.5$  s, middle panels).

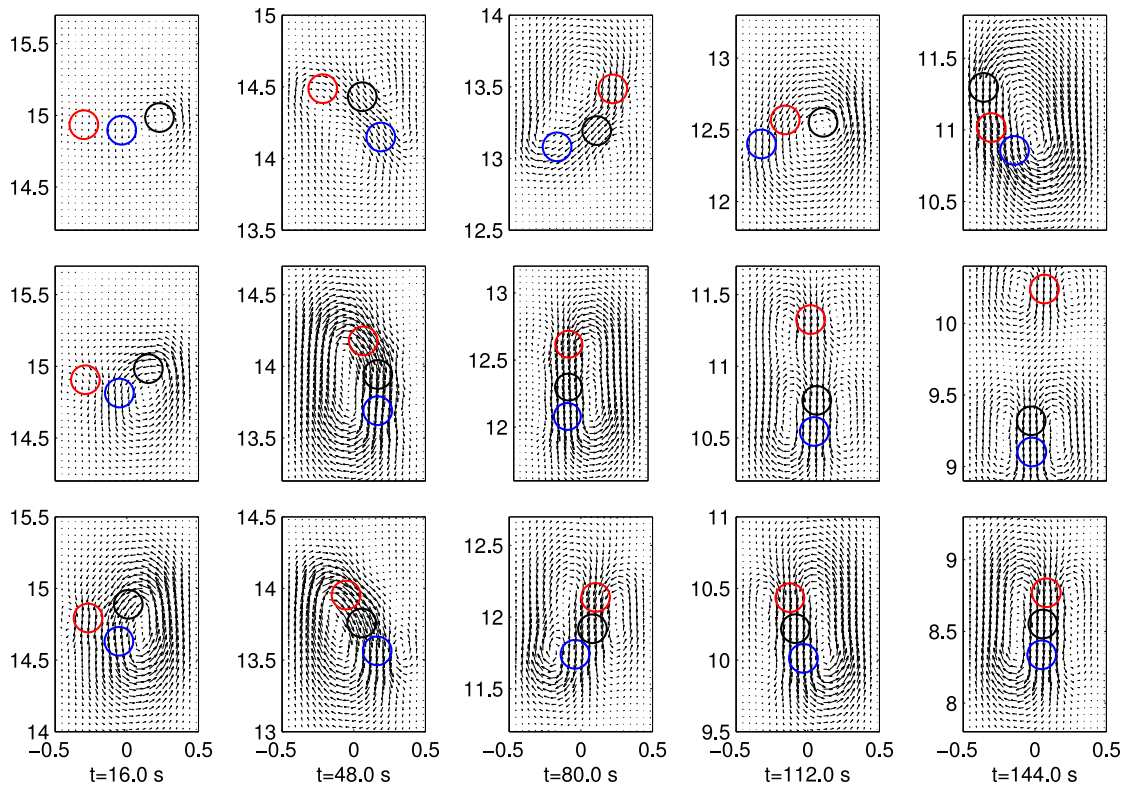


**Fig. 9.** Velocity fields and the interaction of the three particles in a Newtonian fluid (upper panels) and Oldroyd-B fluids with the relaxation time  $r_t = 1.5$  s (middle panels) and 3.0 s (lower panels) at some chosen times. The three particles form a chain along the falling direction only in the Oldroyd-B fluids (middle and lower panels); however, one of three particles breaks the chain to get far away from the chain of the other two particles in the middle panels.

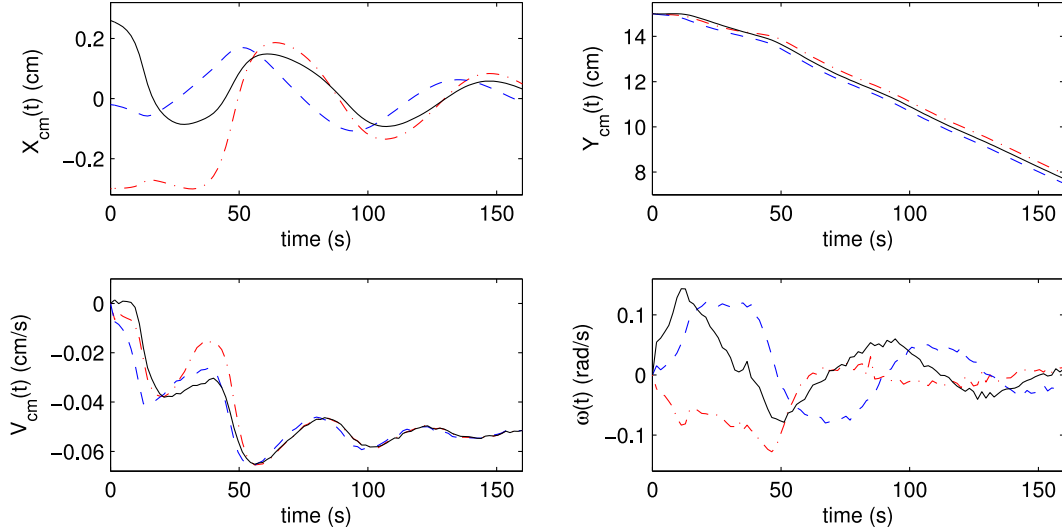


**Fig. 10.** The time evolution of the x (upper-right) and y (upper-left) components of the three particles freely falling in the Oldroyd-B fluid with  $r_t = 3.0$  s, and their descent (lower-left) and angular (lower-right) velocities,  $V_{cm}(t)$  and  $\omega(t)$ . The dash-dotted red lines, the dashed blue lines, and the solid black lines refer to the initially left, middle, and right particles, respectively, see Fig. 9. (For interpretation of the references to colour in this figure legend, the reader is referred to the web version of this article.)

The upper panels of Fig. 10 show the time evolution of the x and y components of the centers  $Y_{cm}(t)$  of the three particles in the Oldroyd-B fluid with  $r_t = 3.0$  s, and the lower panels show their descent (left) and angular (right) velocities,  $V_{cm}(t)$  and  $\omega(t)$ . We can see from the upper panels that the chain of the three particles is formed around  $t = 40$  s which falls approximately on the centerline of the domain. The angular velocities  $\omega(t)$  approach 0, and the descent velocities  $V_{cm}(t)$  are approximately a constant. The average terminal velocity is 0.053 cm/s which

induces  $Re = 0.04$ ,  $De = 0.792$ , and  $E = 19.5$ . Notice the non-smooth fluctuations of  $\omega(t)$  in the lower-right panel, see also Fig. 7. These non-smooth fluctuations of  $\omega(t)$  are likely due to the large penalty stiffness and exist both in Newtonian and Oldroyd-B fluids. One might worry about the non-smooth oscillation introduced into the system by the large value of the penalty stiffness  $K$ . As you can see, however, the fluctuation amplitude seems to be quite small in Figs. 7 and 10 and can be damped out further as the temporal and spatial resolutions are refined.

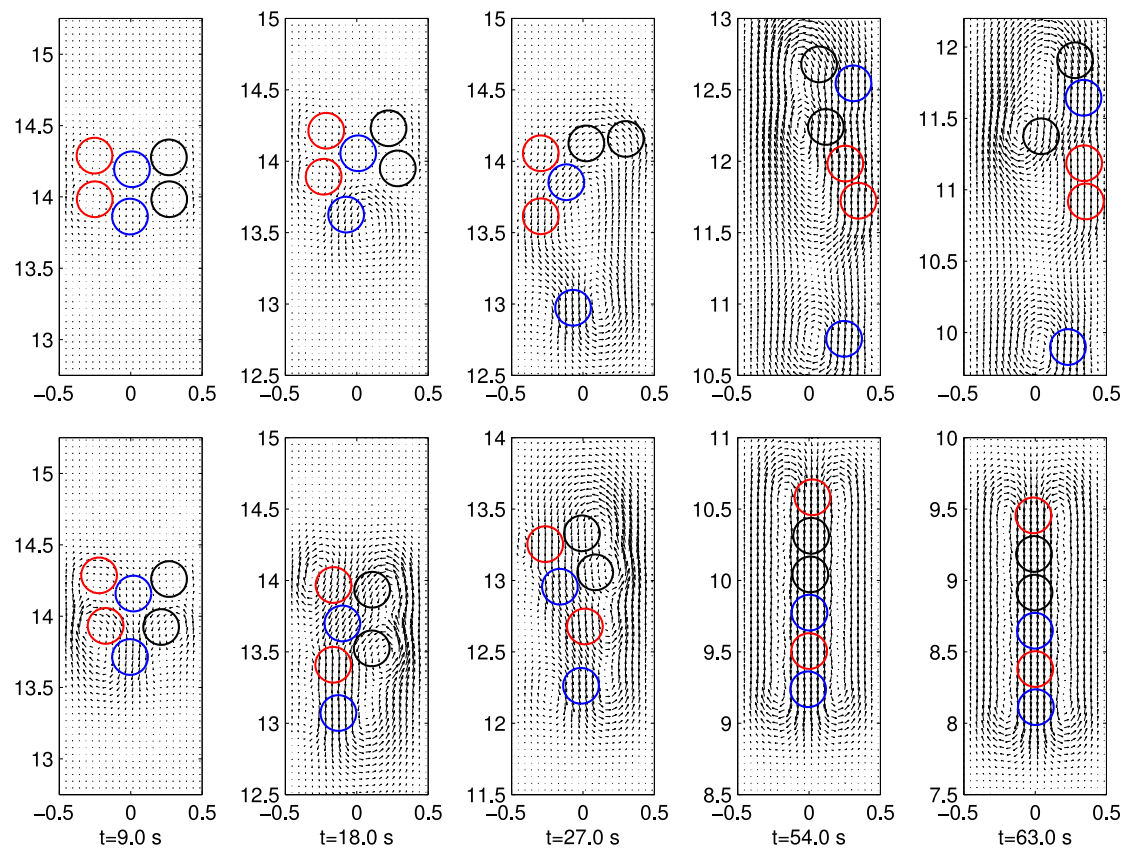


**Fig. 11.** Velocity fields and the interaction of the six particles in a Newtonian fluid (upper panels) and an Oldroyd-B fluid with the relaxation time  $r_t = 1.3$  s (lower panels) at some selected times. The six particles, which form a chain along the falling direction, descend at the centerline of the channel only in the Oldroyd-B fluid (lower panels).

We consider as the final test case six circular particles descending in a channel filled with an Oldroyd-B fluid which has the following properties:  $\rho = 1.0$  g/cm<sup>3</sup>,  $r_t = 1.3$  s,  $\mu_s = 0.0325$  g/(cm·s), and  $\mu_p = 0.2275$  g/(cm·s). Then six identical particles, which have diameter  $D = 0.25$  cm and density  $\rho_L = 1.01$  g/cm<sup>3</sup>, are released at the initial positions  $(-0.27$  cm, 14.0 cm),  $(0$ , 14.0 cm),  $(0.28$  cm, 14.0 cm),  $(-0.28$  cm, 14.3 cm),  $(0$ , 14.3 cm), and  $(0.27$  cm, 14.3 cm). The mesh-width is  $h = 1/128$  cm, and the time step is  $\Delta t = 1.5 \times 10^{-5}$  s.

It is well known that, when the elasticity number  $E$  is larger than the critical value ( $O(1)$ ) and the Mach number  $M$  is less than the critical value ( $O(1)$ ), the particles in this case will form a chain that is parallel to the falling direction [5–7]. Fig. 11 compares the interaction of the six particles in a Newtonian fluid (upper panels) and an Oldroyd-B fluid with  $r_t = 1.3$  s (lower panels). While the particles in the Newtonian fluid scatter and descend close to the wall, those in the Oldroyd-B fluid are lined up along the falling direction at the centerline of the domain, which is comparable to the observations in [7]. The average terminal velocity of the six combined particles is 0.125 cm/s which induces Reynolds number  $Re = 0.12$ , Deborah number  $De = 0.65$ , and elasticity number  $E = 5.4$ .

## 5. Summary and conclusions

We have introduced an extension of the penalty immersed boundary method that can handle a rigid body immersed in an Oldroyd-B fluid. This method conceptually separates the rigid body into two parts, one of which has the mass density of the ambient fluid, while the other one carries the excess mass of the body. The part with the mass density of the ambient fluid is modeled as a part of the fluid, and the other part is

modeled as a rigid body. The two parts are linked by a system of stiff springs, which effectively force their motions to agree.

This approach has the virtue of simplicity. The Oldroyd-B fluid equations are defined and solved on the whole computational domain (including the region occupied by the particles) with constant density and viscosity, which makes it possible to use some efficient numerical solvers such as FFT. (The viscosity within the particle regions has no physical consequences, since the motion there is effectively like rigid body motion anyway.) To simplify the fluid-particle interaction, we virtually decouple the rigid body solver from the fluid equations by introducing the massive boundary  $Y$  which follows the rigid body dynamics and is linked to the fluid dynamics via the massless boundary  $X$ . This form of linkage is done by a spring force that connects  $X$  and  $Y$  in a satisfactory manner and gives feedback to the fluid dynamics. The method is easy to implement as an add-on to any Oldroyd-B fluid solver for the uniform density, uniform viscosity case.

Another advantage of the present piB method is that it can be applied to more general problems of non-Newtonian fluid dynamics of rigid immersed bodies, possibly of complicated geometry or with mass density distributed in a non-uniform manner, either by themselves or in combination with the kinds of elastic immersed boundaries that have always been the application domain of the immersed boundary method.

We have applied this new extension to some benchmark problems, including sedimentation of multiple circular particles and shown that the multiple particles in an Oldroyd-B fluid are lined up along the flow direction, which verifies the known observations and experiments. We have also investigated the effects of the elasticity and wall by releasing a single particle at different distances from the wall and shown that the lateral equilibrium positions of the falling particle depend on the elasticity number, which was also well observed in literature. Additional

validation has been provided in the form of a convergence study, which confirms the expected first-order accuracy of the scheme.

Since the purpose of this paper has been to introduce and illustrate the new method, we have not yet pursued the applications begun here in as much detail as they deserve. For example, two particles settling in a channel filled with a Newtonian fluid go through from steady motions to periodic motions including periodic-doubling and chaotic states as the Reynolds number increases in a low Reynolds number flow regime [36,37]. In an Oldroyd-B fluid, two kinds of particle dynamics are observed: (i) a periodic interaction in a small elasticity number flow, and (ii) the formation of a two-disk chain in a larger elasticity number flow [35]. The dependence of the interaction between two particles on Reynolds, elasticity, and Mach numbers needs further investigations. The sedimentation of particles with various shapes both in 2 and 3 dimensional Oldroyd-B fluids will also be the subject of future work.

## Acknowledgment

Y. Kim was supported by National Research Foundation of Korea Grant funded by the Korean Government (2017R1E1A1A03070636). M.-C. Lai was supported in part by Ministry of Science and Technology of Taiwan under research grant MOST-104-2115-M-009-014-MY3.

## References

- [1] R.P. Chhabra, *Bubbles, Drops, and Particles in Non-Newtonian Fluids*, CRC Press, Boca Raton, FL, 1993.
- [2] G.H. McKinley, Steady and transient motion of spherical particles in viscoelastic liquids, in: D. De Kee, R.P. Chhabra (Eds.), *Transport Processes in Bubbles, Drops, and Particles*, Taylor & Francis, New York, 2nd ed. edition, 2002.
- [3] P.Y. Huang, H.H. Hu, D.D. Joseph, Direct simulation of the sedimentation of elliptical particles in oldroyd-b fluids, *J. Fluid Mech.* 362 (1998).
- [4] D.D. Joseph, Y.J. Liu, Orientation of long bodies falling in a viscoelastic liquid, *J. Rheol.* 37 (1993).
- [5] P. Singh, D.D. Joseph, T.I. Helsa, R. Glowinski, T.W. Pan, A distributed lagrange multiplier/fictitious domain method for viscoelastic particulate flows, *J. Non-Newtonian Fluid Mech.* 91 (2000).
- [6] Z. Yu, N. Phan-Thien, Y. Fan, R.I. Tanner, Viscoelastic mobility problem of a system of particles, *J. Non-Newtonian Fluid Mech.* 104 (2002).
- [7] J. Hao, T.W. Pan, R. Glowinski, D.D. Joseph, A fictitious domain/distributed lagrange multiplier method for the particulate flow of oldroyd-b fluids: a positive definiteness preserving approach, *J. Non-Newtonian Fluid Mech.* 156 (2009).
- [8] J. Feng, P.Y. Huang, D.D. Joseph, Dynamic simulation of sedimentation of solid particles in an oldroyd-b fluid, *J. Non-Newtonian Fluid Mech.* 63 (1996).
- [9] H.H. Hu, N.A. Patankar, M.Y. Zhu, Direct numerical simulations of fluid-solid systems using the arbitrary lagrangian-eulerian technique, *J. Comput. Phys.* 169 (2001).
- [10] Z. Yu, A. Waches, Y. Peysson, Numerical simulation of particle sedimentation in shear-thinning fluids with a fictitious domain method, *J. Non-Newtonian Fluid Mech.* 136 (2006).
- [11] H. Binous, R.J. Phillips, Dynamic simulation of one and two particles sedimenting in viscoelastic suspensions of FENE dumbbells, *J. Non-Newtonian Fluid Mech.* 83 (1999).
- [12] D.D. Joseph, Y.J. Liu, M. Poletto, J. Feng, Aggregation and dispersion of spheres falling in viscoelastic liquids, *J. Non-Newtonian Fluid Mech.* 54 (1994).
- [13] C.S. Peskin, The immersed boundary method, *Acta Numerica* 11 (2002) 479–517.
- [14] C.S. Peskin, Numerical analysis of blood flow in the heart, *J. Comput. Phys.* 25 (1977) 220–252.
- [15] C.S. Peskin, D.M. McQueen, Fluid dynamics of the heart and its valves, in: *Case studies in Mathematical Modeling: Ecology, Physiology, and Cell Biology*, Prentice Hall, Englewood Cliffs NJ, 1996, pp. 309–337.
- [16] Y. Kim, C.S. Peskin, Penalty immersed boundary method with an elastic boundary with mass, *Phys. Fluids* 19 (5) (2007).
- [17] Y. Kim, C.S. Peskin, Penalty immersed boundary method for a rigid body in fluid, *Phys. Fluids* 19 (5) (2016).
- [18] Y. Kim, C.S. Peskin, Numerical study of incompressible fluid dynamics with nonuniform density by the immersed boundary method, *Phys. Fluids* 20 (2008) 062101.
- [19] J.J. Heys, B. Knott, T. Gedeon, Y. Kim, Modeling arthropod filiform hair motion using the penalty immersed boundary method, *J. Biomech. Eng.* 41 (5) (2008) 977–984.
- [20] Y. Kim, S. Lim, S.V. Raman, O.P. Simonetti, A. Friedman, Blood flow in a compliant vessel by the immersed boundary method, *Ann. Biomed. Eng.* 37 (5) (2009) 927–942.
- [21] N.O. Jaensson, M.A. Hulsen, P.D. Anderson, Direct numerical simulation of particle alignment in viscoelastic fluids, *J. Non-Newtonian Fluid Mech.* 235 (2016).
- [22] P. Singh, D.D. Joseph, Sedimentation of a sphere near a vertical wall in an oldroyd-b fluid, *J. Non-Newtonian Fluid Mech.* 94 (2000).
- [23] M.C. Lai, C.S. Peskin, An immersed boundary method with formal second-order accuracy and reduced numerical viscosity, *J. Comput. Phys.* 160 (2000) 705–719.
- [24] D.M. McQueen, C.S. Peskin, Heart simulation by an immersed boundary method with formal second-order accuracy and reduced numerical viscosity, in: *Mechanics for a New Millennium, Proceedings of the International Conference on Theoretical and Applied Mechanics (ICTAM)*, 2000.
- [25] F.H. Harlow, J.E. Welsh, Numerical calculation of time-dependent viscous incompressible flow of fluid with a free surface, *Phys. Fluids* 8 (1965) 2181–2189.
- [26] J.C. Crispella, R. Cortez, D.B. Khismatullin, L.J. Fauci, Shape oscillations of a droplet in an oldroyd-b fluid, *Physica D* 240 (20) (2011).
- [27] D. Goldstein, R. Handler, L. Sirovich, Modeling a no-slip flow with an external force field, *J. Comput. Phys.* 105 (1993) 354–366.
- [28] C. Lee, Stability characteristics of the virtual boundary method in three-dimensional applications, *J. Comput. Phys.* 184 (2003) 559–591.
- [29] Y. Kim, J. Lee, S. Lim, Nodal flow simulations by the immersed boundary method, *SIAM J. Appl. Math.* 74 (2014) 263–283.
- [30] M.C. Lai, *Simulations of the Flow Past an Array of Circular Cylinders as a Test of the Immersed Boundary Method*, Ph.d. thesis, Mathematics, New York University, 1998.
- [31] R. Glowinski, T.W. Pan, J. Periaux, Distributed lagrange multiplier methods for incompressible flow around moving rigid bodies, *Comput. Methods Appl. Mech. Eng.* 151 (1998).
- [32] L. Zeng, S. Balachandar, P. Fischer, Wall-induced forces on a rigid sphere at finite reynolds number, *J. Fluid Mech.* 536 (2005).
- [33] S.A. Poniaev, K.K. Soboleva, A.I. Sobolev, V.V. Dudevlev, G.S. Sokolovskii, Drag coefficient of solid micro-sphere between parallel plates, *J. Phys. Conf. Ser.* 769 (1) (2016).
- [34] J. Feng, D.D. Joseph, R. Glowinski, T.W. Pan, A three-dimensional computation of the force and torque on an ellipsoid settling slowly through a viscoelastic fluid, *J. Fluid Mech.* 283 (1995).
- [35] T.W. Pan, R. Glowinski, Dynamics of two disks settling in a two-dimensional narrow channel: from periodic motion to vertical chain in oldroyd-b fluid, *Phys. Rev. E* 96 (2017) 063103.
- [36] J. Feng, H.H. Hu, D.D. Joseph, Direct simulation of initial value problems for the motion of solid bodies in a newtonian fluid part 1. sedimentation, *J. Fluid Mech.* 261 (1994) 95–134.
- [37] C.K. Aidun, E.J. Ding, Dynamics of particle sedimentation in a vertical channel: period-doubling bifurcation and chaotic state, *Phys. Fluids* 5 (6) (2003) 1612–1621.